



BABEȘ-BOLYAI UNIVERSITY
Faculty of Physics
Doctoral School of Physics



Ph.D. THESIS

SUMMARY

**Characterization of Radiation Field in Particle
Therapy using Pixel Detectors**

Cristina BĂLAN

Thesis supervisor
Prof. dr. Vasile CHIȘ

Cluj-Napoca

2025

Table of Contents

| | |
|--|-----|
| Table of Contents | iii |
| Introduction | 1 |
| 1. Particle therapy | 3 |
| 1.1. Principle of electron radiotherapy | 3 |
| 1.2. Principle of proton radiotherapy | 5 |
| 2. Timepix detectors: design and functionality | 6 |
| 2.1 Timepix detectors | 6 |
| 2.2 Data acquisition and processing | 7 |
| 2.3 Spectral-sensitive particle tracking..... | 8 |
| 2.3.1 Pattern recognition of single particle tracks | 8 |
| 2.3.2 Artificial intelligence – neural network algorithms | 10 |
| 3. Characterization of primary and secondary radiation produced by FLASH electron beams..... | 11 |
| 3.1 FLASH therapy. Current limitations and challenges | 11 |
| 3.2 Material and methods | 11 |
| 3.2.1. MiniPIX Timepix3 detectors: rigid, flex, and bare configurations | 11 |
| 3.2.2. Detectors operations and read-out data | 12 |
| 3.3 Results | 12 |
| 3.4 Discussion and conclusions | 17 |
| 4. Particle tracking, identification, and LET measurements for scattered radiation in proton therapy with metallic implants | 18 |

| | | |
|-----|--|----|
| 4.1 | Management of metallic inserts in head and neck cancer patients..... | 18 |
| 4.2 | Materials and methods | 19 |
| 4.3 | Results | 19 |
| 4.4 | Discussion and conclusions | 25 |
| 5. | Dosimetric impact of Titanium (Ti) implants in proton therapy | 27 |
| 5.1 | Impact of titanium inserts in proton therapy..... | 27 |
| 5.2 | Material and methods | 27 |
| 5.3 | Results | 28 |
| 5.4 | Discussion and conclusions | 33 |
| | General conclusions..... | 34 |
| | Personal contributions included as part of the thesis | 35 |
| | Additional contributions not related to the PhD subject | 38 |
| | Bibliography | 40 |

Keywords: particle therapy; Timepix3 detectors; artificial intelligence; particle discrimination and visualization; UHDR electron beam; titanium implants; scattered radiation.

Introduction

State-of-the-art radiation therapy is represented by one customized treatment plan that delivers the prescribed radiation dose to the target region, trying to minimize the radiation impact on the healthy tissue surrounding the target volume [1]. By using different types of particles (x-rays, electrons, protons, ions) to achieve the therapeutical window, multiple instrumentations and technologies are needed to ensure the accuracy of these long-term treatments [2-5]. The recent discoveries regarding the radiobiological concepts of electrons reflected into the FLASH effect or the superior properties of protons in the matter of dose deposition into the irradiated volume offer a new direction for the latest generation of detectors suitable for dose characterization in these conditions [6-9]. Scattered radiation resulting after the primary beam's interaction with matter in previously mentioned techniques should be explored to expand the knowledge of particle therapy [10-12]. For that reason, a new generation of detectors with a pixelated matrix of a semiconductor component resulted within the Medipix collaboration in the CERN laboratories, offer a multifunctional design for Timepix (TPX) detectors capable of doing dosimetric analyses in the medical field and not only [13-15].

Thesis objectives

Merging the benefits of this new generation of Timepix detectors with artificial intelligence (AI) and machine learning algorithms used in particle identification, the thesis aim is to combine the medical physics knowledge applied in particle therapy with the novelty in detection and dosimetric characterization. For that reason, measurements of dose rates (DR) or particle fluxes, or even complex parameters like linear energy transfer (LET) in electron therapy using high dose rates and in proton therapy with metallic dental

implants in anthropomorphic head phantom are the main topics related to the thesis subject. The research is divided into two parts:

1st. Customized MiniPIX TPX3 (Timepix3) detectors were used in ultra-high dose rate (UHDR) electron beams to measure primary and stray radiation at various positions relative to the incident beam center [16].

2nd. MiniPIX Timepix3 detectors placed behind different phantoms (anthropomorphic head phantom, Plexiglas phantoms) were used to characterize the scattered radiation produced by a proton beam when metallic inserts were inserted in the irradiation field [17], [18].

Exploration of dosimetry parameters for the out-of-field radiation presented in both parts of this thesis represents some valuable knowledge regarding electron and proton therapy that could be transferred to the clinical workflow. We aim to provide a quantification of energy deposition in a clinical electron beam described by a UHDR to test the feasibility of TPX detectors and their potential use in beam commissioning of new FLASH technology. We evaluated the impact of two titanium (Ti) implants like those used in molar replacements over a head and neck cancer (HNC) case.

1. Particle therapy

One of the essential aspects of radiotherapy, regardless of the particle's type, is the dose deposition. At the same time, all uncertainties that affect its delivery directly to the tumor could determine unpredictable results [19]. It is already known that the proton interaction with matter differs entirely from that produced by an electron beam passing through matter [20]. Healthy tissue exposure to incident radiation is unavoidable, so the toxicity levels developed in normal cells are monitored and reported constantly. This kind of radiation is known as out-of-field radiation. The primary beam interacts with the malignant cells and produces secondary particles that can travel across the irradiated body, inducing toxicity [21], [22]. Using innovative detection techniques capable of particle identification, biological and physical implications of particles could determine improved clinical outcomes [23], [24].

To correlate the outcomes of particle therapy with the well-known results obtained with photon-based treatments, a new concept was introduced: relative biological effectiveness (RBE). The concept behind RBE is a correlation between factors such as particle type, beam quality, irradiation geometry, tumor cell response over irradiation, and so on. Particles' ionization density also influences the RBE, so direct linear energy transfer (LET) measurements could predict the impact of this kind of density on the biological response [25].

1.1. Principle of electron radiotherapy

Electron therapy is considered one of the primaries of radiotherapy treatments and has a versatile portfolio for superficial lesions [26]. Modern trends in radiotherapy have shown the possibility of improved tissue response to electron beams if the same amount of dose is delivered significantly faster, using DRs higher than 40 Gy/s [13], [17]. The advantages of this kind of

irradiation are represented by the relationship observed in normal tissue regeneration versus hypoxic levels of tumor cells. Dose deposition across irradiated matter for an electron beam is described by a superficial curve where the negatively charged particles release their energy at the beginning, followed by a fast drop-off [28]. Known as the percentage depth dose (PDD), Figure 1.1 resumes the characteristic dose deposition (%) of different particles (photons, electrons, and protons) once they pass through water (cm). A 6 MV photon and a 12 MeV electron beam release their maximum doses immediately after crossing the interface between two mediums. Compared to electrons, photons could travel continuously through the medium, depositing doses up to 30 cm. On the other side, as Figure 1.1 shows, the reason for choosing an electron-based treatment for skin lesions or other superficial tumors is their short travel in water of approximately 6 cm.

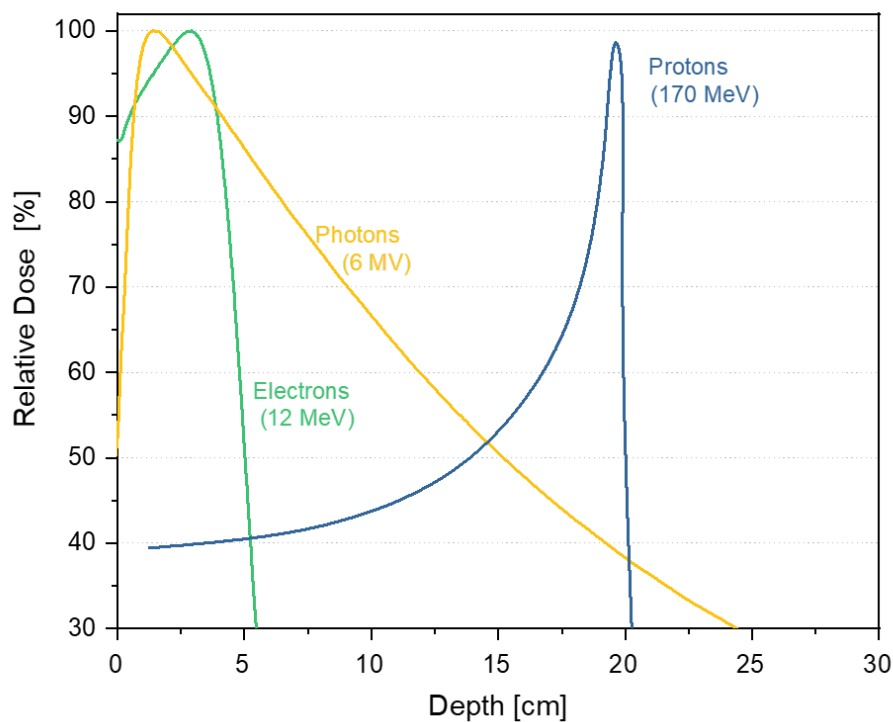


Figure 1.1 . Comparative relative dose deposition of three different beams (electrons – in green; photons – in yellow; protons – in blue) passing through water

This behavior results from charged particle interactions with atoms in the irradiated volume. Unlike uncharged particles like photons, electrons and protons cause direct ionization. The electron beam mainly releases energy by colliding with other electrons and the atom's nucleus. Incident electrons will produce a cascade of ionization and excitation due to the numerous scatterings suffered at the beginning of their path into the matter [29].

1.2. Principle of proton radiotherapy

There are specific pathologies in which proton therapy has superior benefits in cancer management. Two examples in this direction are represented by head and neck cancer (HNC) and pediatric oncology patients [30-32].

The accelerated protons penetrate the irradiated volume with minimal energy release until they reach a Bragg peak (BP), where all protons release their entire energy, and no dose is reported after that [33]. Compared to previous therapies based on electrons and photons, these particles are attenuated when crossing the medium, resulting in significant dose deposition over the entire irradiated volume. Conversely, the situation is entirely different in proton therapy compared to the electron or photon-based treatments, when particles are stopped at their end range, and a minimal exit dose is reported [34]. The proton path is described by a linear path at the beginning and starts to be slowed down by the interactions with other particles from the irradiated medium. The maximum energy is released as the BP shown in Figure 1.1 **Error! Reference source not found.** [25].

2. Timepix detectors: design and functionality

2.1 Timepix detectors

A new generation of radiation detectors is developed based on a novel design in the Medipix collaboration, one of the CERN laboratories. Particle detectors combining a read-out chip with a semiconductor component represent the hybrid pixelated detectors capable of imaging, detecting, and counting events that impressed the sensor's surface [13]. Blending the technology used in high energy physics and photon counting methodology, the resulting detector proved efficient in multiple applications like space dosimetry, particle tracking, colorful CT images, and even radiotherapy [9], [35-37]. With a high granularity level due to the total number of pixels, the Timepix detector possesses an active area of $14 \times 14 \text{ mm}^2$ [35], [38]. The main benefits of these pixelated detectors are represented by [35], [38-41]:

- noiseless detection
- spectral-tracking analysis
- wide per-pixel range of counting and energy levels
- quantum-imaging sensitivity
- photon-counting camera
- room-temperature stability
- miniaturized readout electronics
- online visualization of single particle track

According to Figure 2.1 a, a semiconductor sensor of variable thickness is usually made from different materials is bump bonded to the Timepix read-out chip [35], [42].

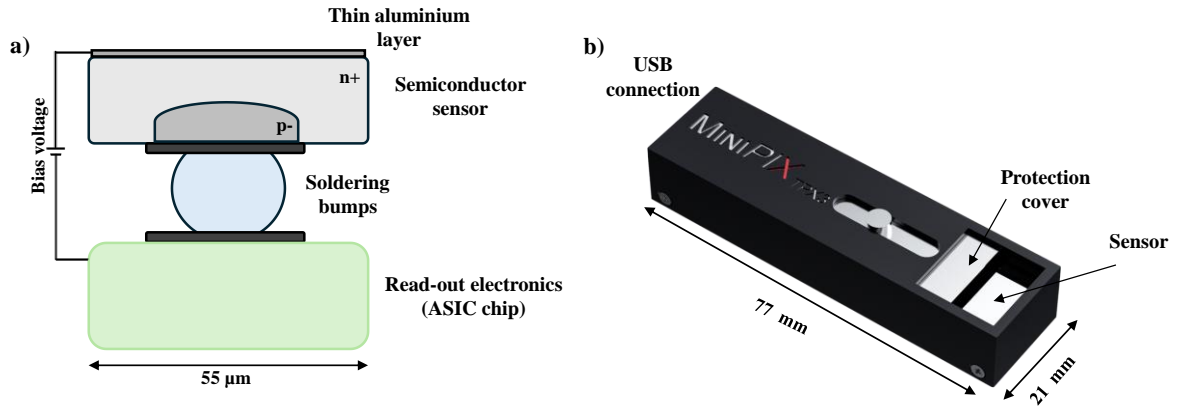


Figure 2.1 a) One-pixel representation from the Timepix chip. A thin aluminium layer covers the semiconductor sensor of variable thicknesses, while a bump solder sticks the sensor to the surface of the read-out component. Each pixel from the square matrix of 256 pixels (total number of pixels: 65536) is described by a pitch of $55\ \mu\text{m}$ b) MiniPIX Timepix3 detector with a total length of 77 mm and only 21 mm width with a direct USB-type connection to supported devices. Adapted from: [9], [40].

Once a particle crosses the sensitive volume of the Timepix, the deposited energy of the particle is distributed over many pixels, forming a cluster [35]. For a precise evaluation of deposited energy produced by incident particles on the sensor's level, the charged sharing effect between pixels and the distance needed for charge collecting should consider the bias level [43], [44].

Data processed in this thesis was measured with various generations of Timepix detectors operated and readout with the miniaturized and room-temperature MiniPIX electronics produced by [ADVACAM](#) (Prague, Czech Republic) [45]. Figure 2.1 b is displaying a MiniPIX Timepix3 detector.

2.2 Data acquisition and processing

Timepix detectors are known for their hybrid design, including semiconductor materials and read-out electronics to collect real-time data. Designed with digital counters, amplifiers, and amplitude discriminators in the read-out electronics of the ASIC chip dedicated to the Timepix detectors, the

signal originating from each pixel could be operated in various modalities, as follows [46], [47]:

- Event counting
- Time over threshold (ToT) or energy mode
- Time of arrival (ToA) or time mode
- Masked

Deposited energy determination in Timepix detectors results from direct charge measurement in each pixel. During the particle interactions with the sensor, some of the pixels will be excited during the energy transfer, and this fingerprint path created at the sensor's level is known as a cluster [35]. Going further with data processing, visual reconstruction, spectrometric analyses, and particle tracking through the sensor thicknesses are needed to characterize the radiation field comprehensively. To evaluate a cluster track, by morphological and spectral perspectives, some parameters are required for further steps of processing [35]:

- cluster area
- deposited energy (E)
- roundness
- length (L)

With specific morphologies described by multiple combinations of parameters mentioned above, each particle could be identified and described using this class of detectors with high resolution in particle identification.

2.3 Spectral-sensitive particle tracking

2.3.1 Pattern recognition of single particle tracks

Based on individual tracks, groups of particles are identified, and their qualitative, combined with quantitative evaluation, gives information regarding the radiation field composition [15], [35]. Figure 2.2 shows the differences

between cluster morphologies registered on a Si sensor of a Timepix3 detector with 500 μm sensor thickness. The measurement was done in an out-of-field region using an incident proton beam. Presented in two-dimensional (2D), the clusters symbolize the deposited energy created on the pixelated matrix's surface by four particles: electrons, ions, protons, and photons. The particles could be easily discriminated based on their roundness level and released energy on the sensor's surface.

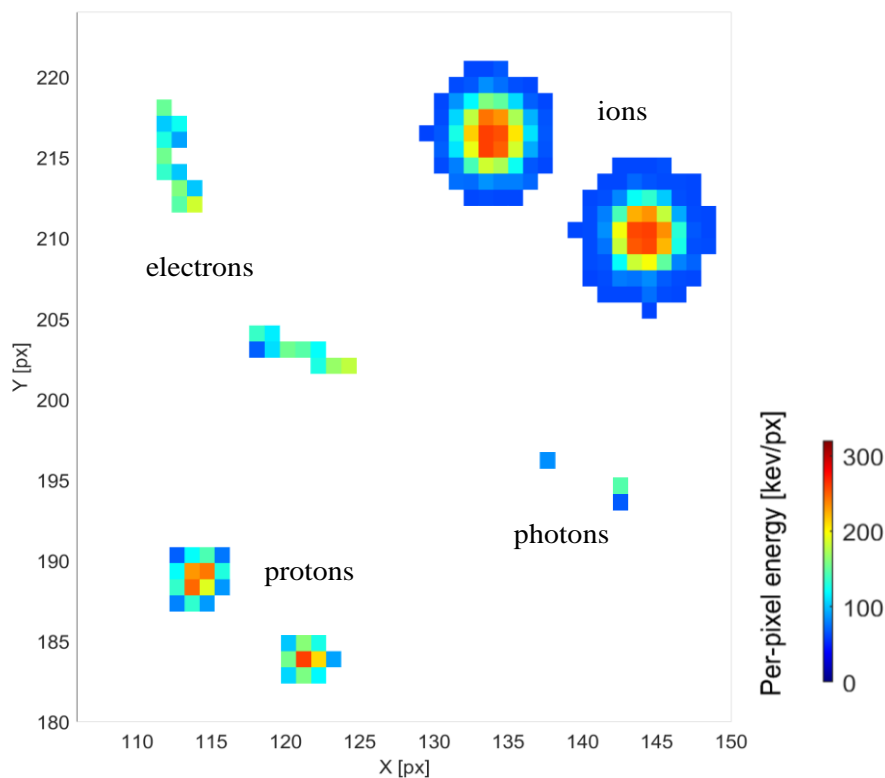


Figure 2.2 Particle tracking in a Timepix3 detector with a Si sensor of 500 μm thickness – selected region of the sensor surface. A 2D representation of the deposited energy of four particle types: electrons, ions, protons, and photons, measured in a mixed radiation field produced by an incident proton beam. Different patterns are created by the incident particle based on their class on a selected region of the detector (2.31 x 2.31 mm^2)

2.3.2 Artificial intelligence – neural network algorithms

Combining morphological aspects with the spectrometric properties of each cluster is one of the main concepts of the DPE (Data Processing Engine) platform developed by [ADVACAM](#) [48]. Artificial intelligence, based on machine learning algorithms, are trained models to recognize patterns in radiation field decomposition by particle identification [15], [17], [48]. Integrated Python scripts from the DPE software are used to fully process data by applying per-pixel correction and calibration files, clustering, particle identification, and physical properties calculations.

Particle classification and radiation field recognition are essential analyses done during data processing. Using an AI interface, a neural network (NN) infrastructure was trained in a well-known radiation field to discriminate particle types [48]. Thus, raw data was decomposed properly by merging the morphological and spectral concepts of events with the machine learning algorithms imposed in the NN concept [15], [35].

The statistical accuracy of AI NN algorithms used during processing, resulted into identifying three classes of particles:

- protons
- electrons & photons
- ions (referring generally to high-energy protons, fast and thermal neutrons)

3. Characterization of primary and secondary radiation produced by FLASH electron beams

3.1 FLASH therapy. Current limitations and challenges

Some aspects regarding the dosimetry of FLASH radiotherapy should be considered when a radiation detector is proposed for dosimetric measurements in FLASH-like beams [49]:

- dose rate dependency
- spatial resolution
- time response

This study proposes prototypes of the MiniPIX Timepix3 detectors for dose-rate and particle fluxes evaluation in electron beams to fill the gaps between existing literature and technical transfer to the clinical domain. This research aims to evaluate the feasibility of the customized Timepix3 detectors in conditions imposed by the ultra-high dose rates of electron beams. For that reason, multiple configurations of sensors were used to quantify the physical parameters like radiation signal, dose rates, and particle fluxes relative to the time of arrival for primary and scattered radiation resulting from an accelerated electron beam in a microtone unit [16].

3.2 Material and methods

3.2.1. MiniPIX Timepix3 detectors: rigid, flex, and bare configurations

Multiple customized versions of the MiniPIX Timepix3 detectors were proposed for this experiment. With various MiniPIX Timepix3 detectors, measurements were taken in the primary electron beam, followed by some measurements in scattered radiation at different lateral distances. In the proposed version of the Flex TPX3, the metallic inserts have been removed and

replaced with carbon or plastic-related materials. With a detachment cable of 5 cm, the sensitive component of the TPX3 is moved from the read-out electronics part to minimize any internal scattering, increasing the internal shielding level of the detector itself [16]. An extruded graphite support was used as a mounting system for the TPX3 sensor assembly [16].

3.2.2. Detectors operations and read-out data

Conducting experiments with higher dose rates, the detector's operations should be adapted to the incident radiation characteristics. Using a TPX3 detector, both energy and time could be simultaneously measured by both channels from each pixel design. The incident particle fluxes are proportional to the dose rates used during the irradiation. For that, in UHDR beams, the number of particles that reach the detectors could exceed 10^5 particles·cm⁻²·s⁻¹ [16], [50]. According to the operational design, the read-out data should be delivered as frames if the conditions of higher particle fluxes are used during the experiment [16].

3.3 Results

a) Measurements in primary electron beam – Bare MiniPIX Timepix3 flex

The flexible version of the TPX3 without a sensor was tested by placing it directly in a primary electron beam of 19.2 MeV operated in UHDR pulses. The bare detector was inserted inside the bunker before the electron beam and tested in DR up to 2000 nA (~ 80 Gy/s). The responses of both channels possessed by the ASIC chip for the bare TPX3 in flexible design were measured in a wide range of DR. With two separate channels, one for charge measurements and one for events counting, results highlight the superior sensitivity of the channel dedicated to the charge measurements [50], [51]. With these results, the bare

detector controlled in a positive setting could be successfully used in UHDR electron beams to quantify radiation signals and events.

The detailed response of the bare detector in the primary electron beam operated in UHDR pulses at different intensities is presented in Figure 3.1. Two irradiations in the same setup were planned considering the positive and negative voltage applied to the ASIC chip. Represented in black, the negative configuration of the motherboard exhibits a linear trend for both radiation signal and detected events for DR up to 500 nA (~ 20 Gy/s). Increasing the DR of the pulsed electron beam to more than 1250 nA to reach the FLASH conditions, the negative configuration of the ASIC chip got saturated. When the negative settings are used, the number of events in DR, more than 10^3 nA, gets saturated, and no more than 10^7 events are reported.

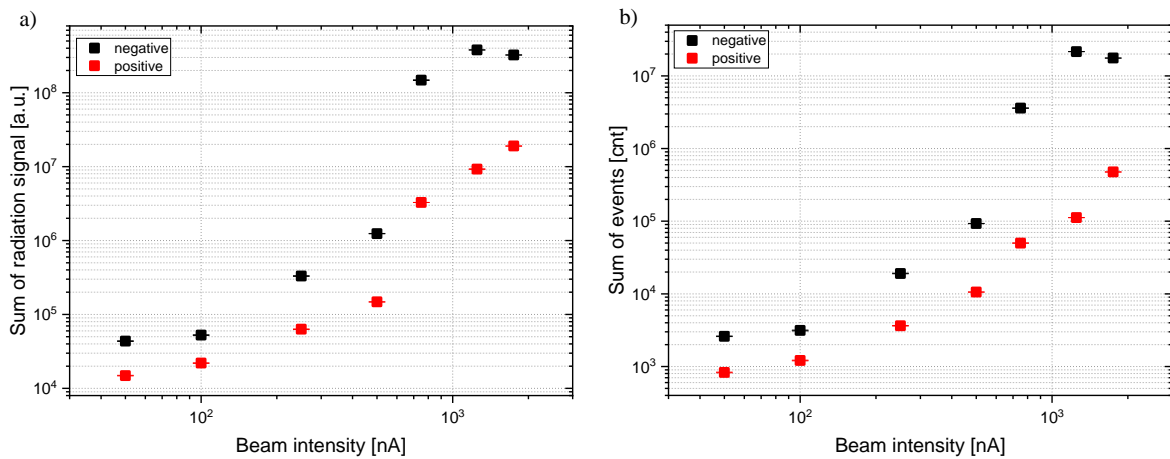


Figure 3.1. Sum of a) radiation signal and b) events measured with TPX3 in flex design without sensor, placed in primary electron beam collimated, operated at different intensities from the UHDR region collected in 60 s from the entire matrix of pixels ($k=1$). The motherboard of the TPX3 flex detector was controlled in both configurations: negative (black) and positive (red)

Using beam intensities up to 1750 nA (~ 70 Gy/s) confirmed the reliability of the TPX3 in the proposed configuration, making them a proper option as detection devices for FLASH-like electron beams.

b) Measurements in scattered electron beam – MiniPIX Timepix3 rigid

One TPX3 in rigid design with a Si sensor of 500 μm was used to monitor the particle fluxes and DR of scattered radiation generated by an electron beam with a nominal 23 MeV energy. A 1 cm PMMA plate was inserted into the irradiation bunker, perpendicular to the electron beam direction to filter out low energy particles. The detector was placed behind the PMMA plate at 10 cm distance laterally from the beam core. Variation of incident electron beam starting from 100 nA (4 Gy/s) and achieving up to 1000 nA (40 Gy/s) was delivered into the irradiation setup[16].

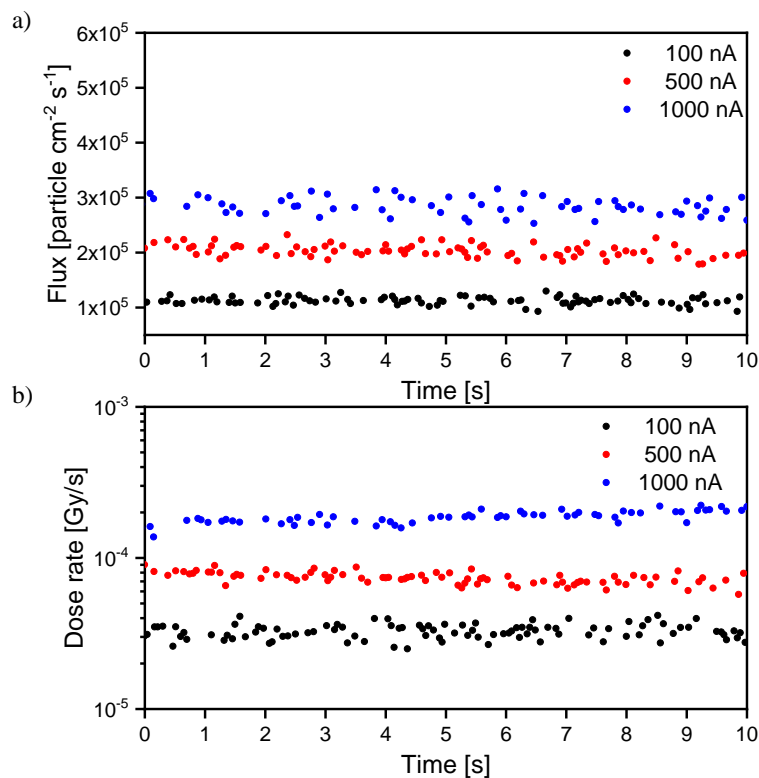


Figure 3.2 Particle fluxes (a) and dose rates (b) measured with a TPX3 rigid detector with a Si sensor of 500 μm produced by one 23 MeV electron beam operated at three different intensities from the UHDR spectrum ($\sim 100, 500,$ and 1000 nA). The detector was mounted behind 1 cm of PMMA plate perpendicular to the beam direction at 10 cm lateral distance [16].

As presented in Figure 3.2, the lateral radiations produced by the electron beam at three intensities were compared in particle fluxes and dose rates. The

background was subtracted from the data during the processing to quantify the scattered radiation produced only by the pulses. A linear response was obtained for particle fluxes for all beam intensities.

The TPX3 rigid detector was set to measure the same variables of scattered radiation but in a low-intensity beam, approx. 50 nA. 8 cm of PMMA plate was introduced to increase the spreading of the incident electron beam (significant decrease in energetic levels of scattered particles). The MiniPIX TPX3 detector with the 500 μm Si sensor was mounted at six different distances from the beam center: 6, 7, 8, 11, 14, and 16 cm. Figure 3.3 shows the particle fluxes (a) and DR (B) for scattered radiation for all six distances. Once the distance between the detector and the center core of the primary beam is increased, particle fluxes and DR of the scattered radiation decrease [16].

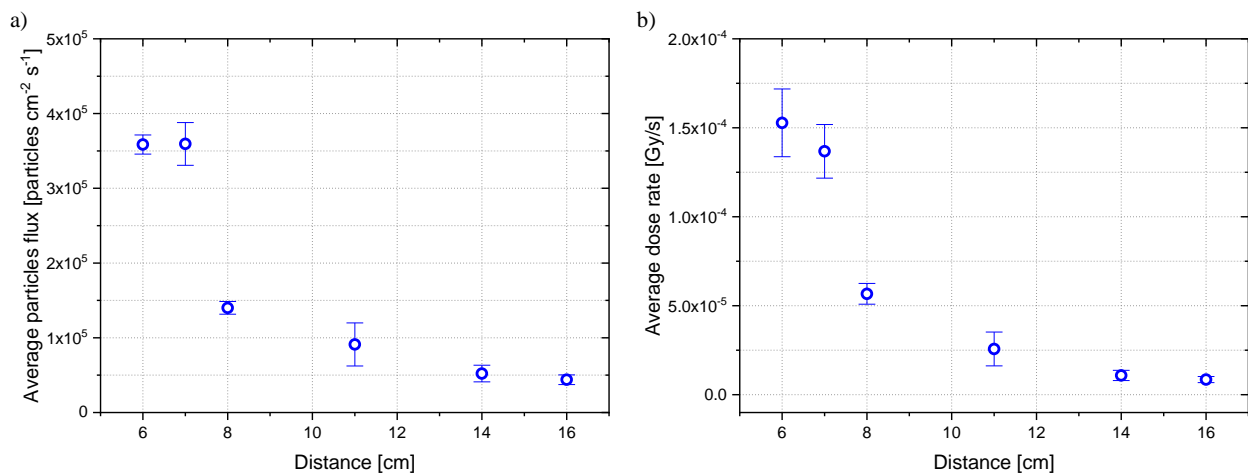


Figure 3.3 Average values for particle fluxes (a) and dose rates (b) produced by a 23 MeV electron beam with an intensity of ~ 50 nA behind one PMMA plate of 8 cm to filter out the high-energy components. The detector was moved laterally to the beam direction at six different positions: 6, 7, 8, 11, 14, and 16 cm from the beam center. The averaged data ($k=1$) presented was collected in 10 s. Adapted from: [16]

c) Measurements in scattered electron beam – MiniPIX Timepix3 Flex

The flexible version of the MiniPIX Timepix3 detector was exploited to facilitate the measurements in UHDR beams. Once the FLASH therapy uses

highly energetic particles delivered in a pulse-based modality, the TPX3 Flex detectors proved themselves suitable as measuring devices in conditions imposed by UHDR beams. Therefore, two flexible detectors with a 100 and 500 μm Si sensor were inserted 10 cm lateral to the beam core to monitor the radiation produced by the Microtron at different DRs behind 1 cm of PMMA plate. To ensure the reliability of the TPX3 Flex in UHDR beams delivered in pulse sequences, the DR of the incident electron beam was constantly increased to cover a wide range of particle densities, from low DR (2 Gy/s) up to FLASH DR (40 Gy/s).

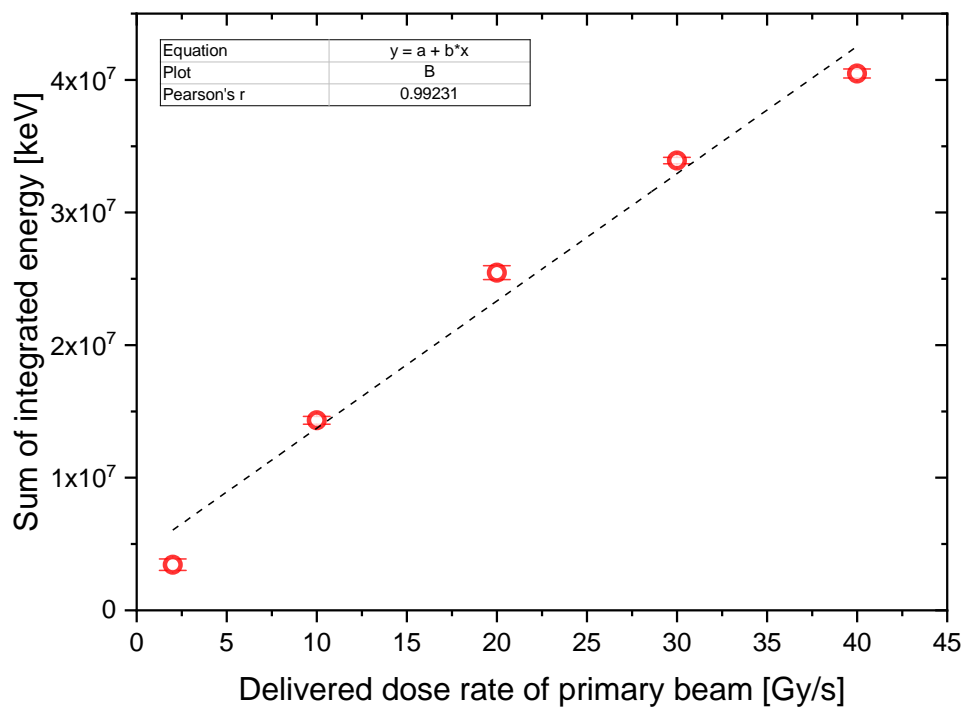


Figure 3.4 The integrated energy of scattered radiation deposited by all events in 0.5 ms at different primary electron beam dose rates measured with a TPX3 Flex with 100 μm Si sensor. The detector was placed 10 cm lateral to the beam's core behind the 1 cm PMMA block. Five DRs of 2, 10, 20, 30, and 40 Gy/s delivered electron pulses into the system.

The linearity of the detector's response regarding the DR increase is highlighted by Pearson's R-value of 0.99231, as Figure 3.4 presents. The detector remained functional throughout the entire irradiation, detecting approximately $4 \cdot 10^7$ keV of deposited energy by all events registered by the sensor at 40 Gy/s in the primary beam.

3.4 Discussion and conclusions

A prototype of the TPX3 detector was proposed as a radiation camera suitable for measuring UHDR beams like those used in FLASH therapy. Mixed tests were conducted during this study to evaluate the feasibility of both detectors, flexible and rigid design, in high intensities of an electron beam in primary and scattered radiation measurements.

Using electron beams delivered in pulses with UHDR, the TPX3 detector, known as the bare detector without any semiconductor component, was successfully tested for in-field measurements.

Visualization of integrated energy deposition of all events measured in DR up to 40 Gy/s of the flexible version of the TPX3 with two different thicknesses emphasizes the dependency of measured data on the sensor's volume.

Furthermore, the TPX3 could successfully measure the scattered radiation in UHDR starting from 6 cm lateral to the beam's center.

The proposed methods of beam characterization in UHDR for electron-based radiotherapy using clinically equivalent energies summarize the statistical impact of the DR and the feasibility of the TPX3 detector in FLASH therapy [16].

4. Particle tracking, identification, and LET measurements for scattered radiation in proton therapy with metallic implants

4.1 Management of metallic inserts in head and neck cancer patients

Proton therapy is considered one of the most viable options for head and neck cancer (HNC) patients due to the proton's dose deposition characteristics. The abrupt fall-off of the delivered dose close to the tumor edge offers a superior dose conformality and a drastic dose reduction to the organs at risk [28], [31], [52], [53].

This chapter presents a characterization of scattered radiation with particle decomposition based on their morphological and spectral properties. It is combined with LET calculations for an HNC case treated with proton therapy when metallic inserts are present in the irradiation field. An anthropomorphic head phantom with two Ti implants placed in the center of the target volumes was used for that. Using a CT scan of the phantom, a proton-based treatment plan was configured in the in-house developed TPS for two irradiations but with different methodologies. One method implies the incorporation of the metallic inserts into the mandibular region, and the other to replace the metallic ones with tissue equivalent (TE) inserts [17].

Scattered radiation dissemination was done with a MiniPIX Timepix3 placed beyond the SOBP. By means, the evaluation consists of particle discrimination and their contribution to the LET spectra in both irradiations. Performing single particle tracking and collecting spectral fingerprints of the secondary and subsequent generation of particles, the overall impact of the metallic implants into a proton treatment for a head and neck case is highlighted [17].

4.2 Materials and methods

An anthropomorphic head phantom with densities equivalent to the human head was used to create a proton plan when two dental implants were inserted into the setup. The methodology proposed in this study involves two irradiation scenarios using the same experimental setup: one with metallic inserts implanted into the phantom and the other with tissue-equivalent (TE) plastic inserts. One planning target volume (PTV) was contoured on CT images of the phantom, with the Ti implants centered inside the irradiation volume. A 3D conformal plan was created by inserting one perpendicular 170 MeV proton beam (irradiation angle: 90°). During the measurements, the delivered dose obtained during the plan optimization was not prioritized, meaning that the plan was used only for conformational reasons during both exposures, with Ti implants and TE inserts, respectively.

With characteristic design, one TPX3 rigid pixelated detector with a Si sensor was mounted near the anthropomorphic head phantom to analyze the impact of those two inhomogeneities in a proton-based plan for a head and neck case [9].

4.3 Results

Particle recognition in mixed radiation field using AI NN model

The complex field of radiation was analyzed using artificial intelligence (AI) neural network (NN) models developed to resolve the complexity of this kind of radiation. Three groups of particles were generated: protons, electrons with photons, and ions with fast neutrons [17], [48]. Results of these NN models from the Data Processing Engine (DPE) are presented in Figure 4.1 for both cases, with metallic inserts in the first column and tissue equivalent inserts in the second column. As displayed in Figure 4.1 a, the spectral deposition of 200 particles from the stray radiation was deconvoluted using the AI NN algorithm.

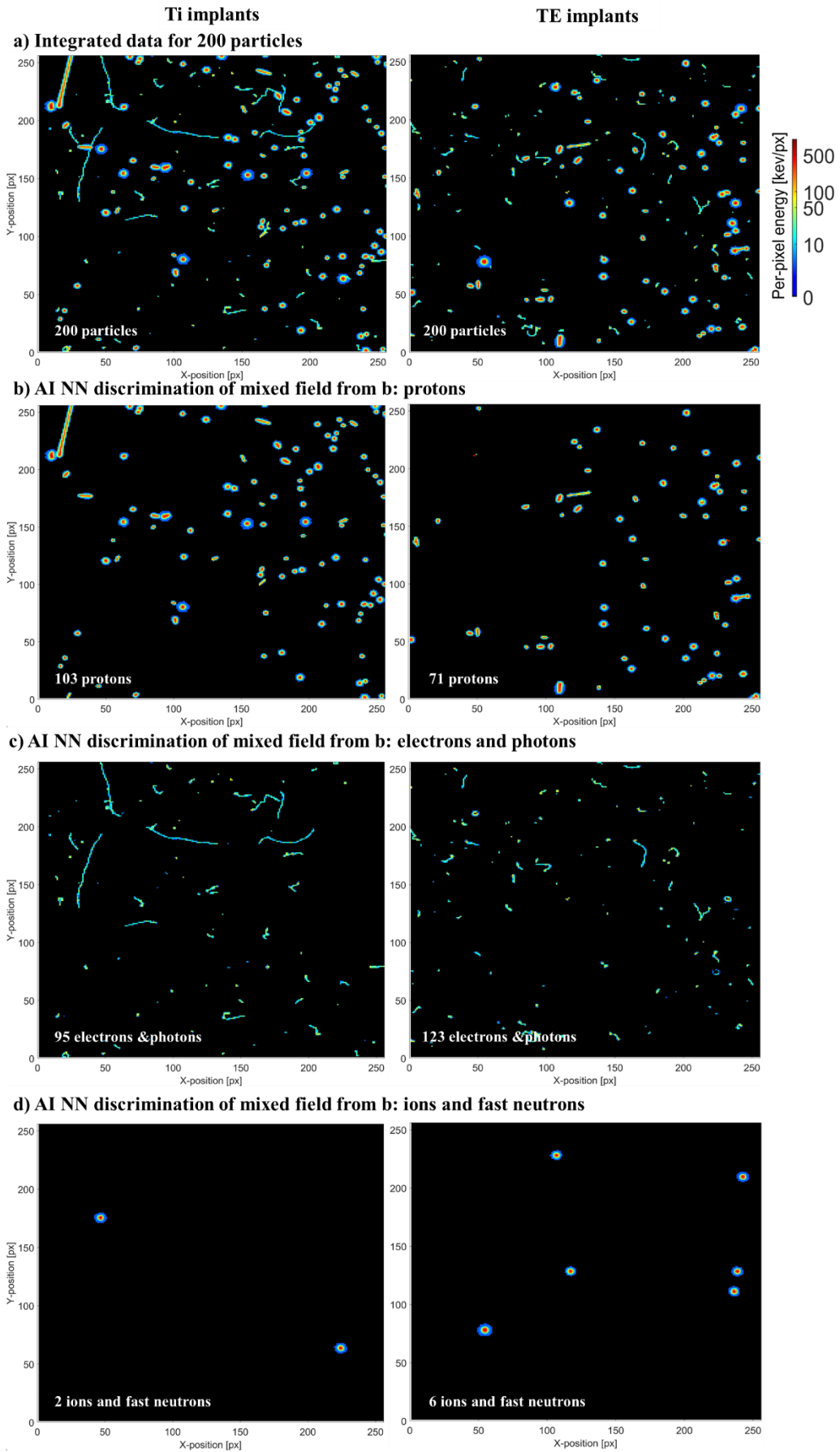


Figure 4.1 Particle decomposition based on morphological and spectral properties of each cluster. The mixed radiation decomposition for measurements done with Ti implants (first column) and tissue equivalent materials (second column) produced behind SOBP. The entire matrix of pixels is represented for the TPX3 with Si sensor. a) 200 particles were filtered and decomposed as follows: b) protons, c) electrons with photons, and d) ions, [17]

The electrons and photons for both sensor positions represent the most predominant group in the stray radiation. Placing the TE inserts in the phantom creates more light-energy particles, more than 10% difference in their contribution to the total scattered radiation, than when Ti inserts were present. The situation is different when Ti implants are inserted in the head phantom. Up to 45% more protons were detected in the perpendicular position of the Si sensor regarding the incident beam direction, facing a reduction to 32% when the metallic inserts were removed and changed with the TE inserts. Placing metallic implants into the irradiation field is emphasized by the proton's contribution to the mixed field of radiation because of the primary proton's interaction with this kind of high-density materials. Detecting ions and fast neutrons is low in the proposed setup, reporting values above 2% in the perpendicular position and below 1% when the sensor is at 60°. There are some limitations in the Si sensor of the TPX3 regarding the neutron's detection, and dedicated converters must be attached to the sensor level to detect this type of particle.

LET spectra of stray radiation

By analyzing the LET spectra of resulting particles produced behind the SOBP, closed to the head phantom with metallic and tissue equivalent inserts, the impact of such inserts on proton treatment for a head and neck case can be evaluated.

The proposed methodology describes the LET spectra of scattered radiation distal to the SOBP for AI NN decomposed radiation field as presented in the previous sections. The LET(water) measurements were derived from the

corresponding LET(Si) calculation values. Figure 4.2 resumes the LET(water) spectra for 35k particles from the mixed field of radiation detected with a TPX3 with a Si sensor positioned perpendicular, at 0° (red) and 60° (blue) relative to the incident proton beam. Increasing the detector's field of view could enhance the discrimination power [35], [43]. Normalization was applied to the data presented to correlate the number of events for each setup. The maximum number of counts was determined for both dental inserts and divided according to their maximum value. The solid line represents the LET values of the measurements performed with Ti implants, while the translucent line was chosen to represent the data sets collected with the TE inserts. The three groups of particles were separated from the mixed radiation field in both scenarios, and their LET corresponding spectra are shown separately: proton (Figure 4.2 b), electrons with photons (Figure 4.2 c), and ions (Figure 4.2 d) [17].

Scattered electrons and photons were the predominant particle type with LET below $1 \text{ keV}/\mu\text{m}$ for the perpendicular position of the Si sensor and below $1.5 \text{ keV}/\mu\text{m}$ for the angular, as Figure 4.2 c shows. The counts reported in both setups exhibit the same trend regardless of Ti or TE inserts' presence in the target volume [17].

Following the LET values, the AI NN algorithms recognized the protons as part of the mixed field of radiation with a large spectrum of LET, starting from $0.5 \text{ keV}/\mu\text{m}$ and reaching values up to $7.5 \text{ keV}/\mu\text{m}$. As described by a wide broad of values, most of the protons detected by the TPX3 sensor deposited their energy per length unit around $1.5 \text{ keV}/\mu\text{m}$ when the sensor was oriented at 0° . For the same position of the sensor, by placing the metallic inserts in the center of the PTV, more protons with low LET are formed inside the scattered radiation, as presented by the red solid line in Figure 4.2 b.

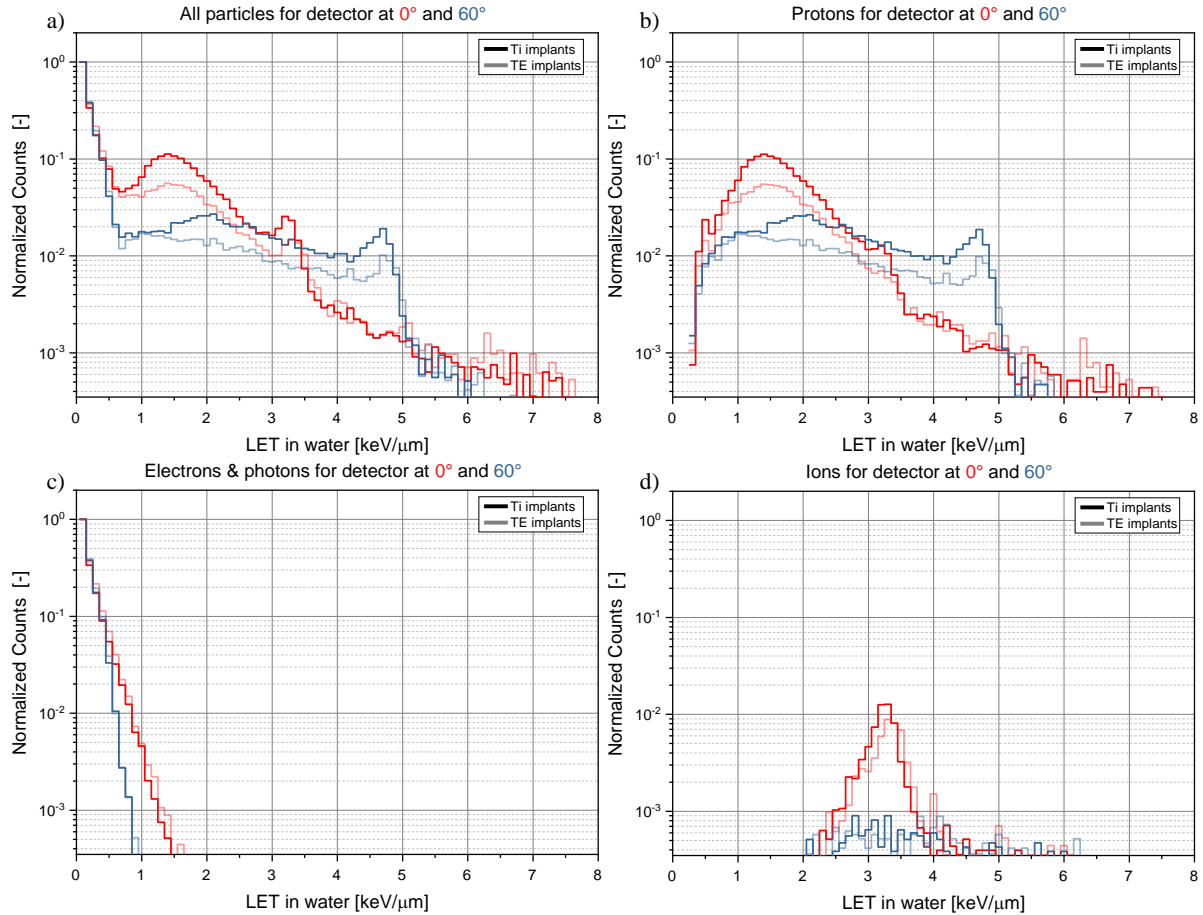


Figure 4.2 The LET in water (LET water) spectra of 35k particles from the stray radiation produced by the incident proton beam when crossing the head phantom with two types of dental implants: Ti implants (bold line) and tissue equivalent (translucent line) for two angular positions of the TPX3 detector with Si sensor 0° (in red) and 60° (in blue). LET spectra in water for the decomposition done by the AI NN algorithms: b) protons, c) electrons and photons, and d) ions [17]

The spectral information collected in both cases exhibits the same trend and shape regardless of titanium presence in the target volume by measuring the LET derived in water with multiple angular positions. Without any shifts reported in the maximum values of the LET in water, no proof indicates the impact of the metallic inserts in this setup over the energy deposition at the sensor level [17].

Particular attention is needed for energetic proton interactions around the Bragg peak. This category of protons is involved in nuclear interaction and inelastic collisions when the maximum energy deposition at their end path through matter is reached. Interacting with densities from the anthropomorphic head phantom when no metals were placed inside the target volume, incident protons create secondary electrons and prompt photons [33], [54], [55].

The ions represent the last category of particles identified by the AI NN algorithms in the out-of-field radiation. These particles are the nuclear results of nuclear interaction between Ti implants and incident protons in the Bragg peak [33]. With LET(water) values starting from 2 up to 6.3 keV/ μm for both Si sensor orientations, there is no connection between Ti inserts and induced enhancement of these high inhomogeneities regarding ion's influence over the proton treatment proposed in this experimental setup [17].

Directional maps and spectral tracking of scattered protons

This study focuses on the impact of high-LET particles from the out-of-field radiation that could affect healthy tissue. For this reason, special attention is given to the scattered protons, whose contribution to the LET is described by a wide range of values as previously described. Individual classification of these protons was done by combining the spectral and morphological aspects with the directional information into two classes: low and high-energy protons. Based on each pixel's spectral sensitivity and tracking response, directional maps of both categories of protons were created with Ti inserts and plastic ones and presented in Figure 4.3 [17], [41].

The directional maps highlighted patterns and distinctions regarding measurements performed with dental implants versus those with TE inserts. Different distributions with specific patterns in lateral spread and relative yield, both horizontal and vertical, could be correlated with the presence of metallic implants [17].

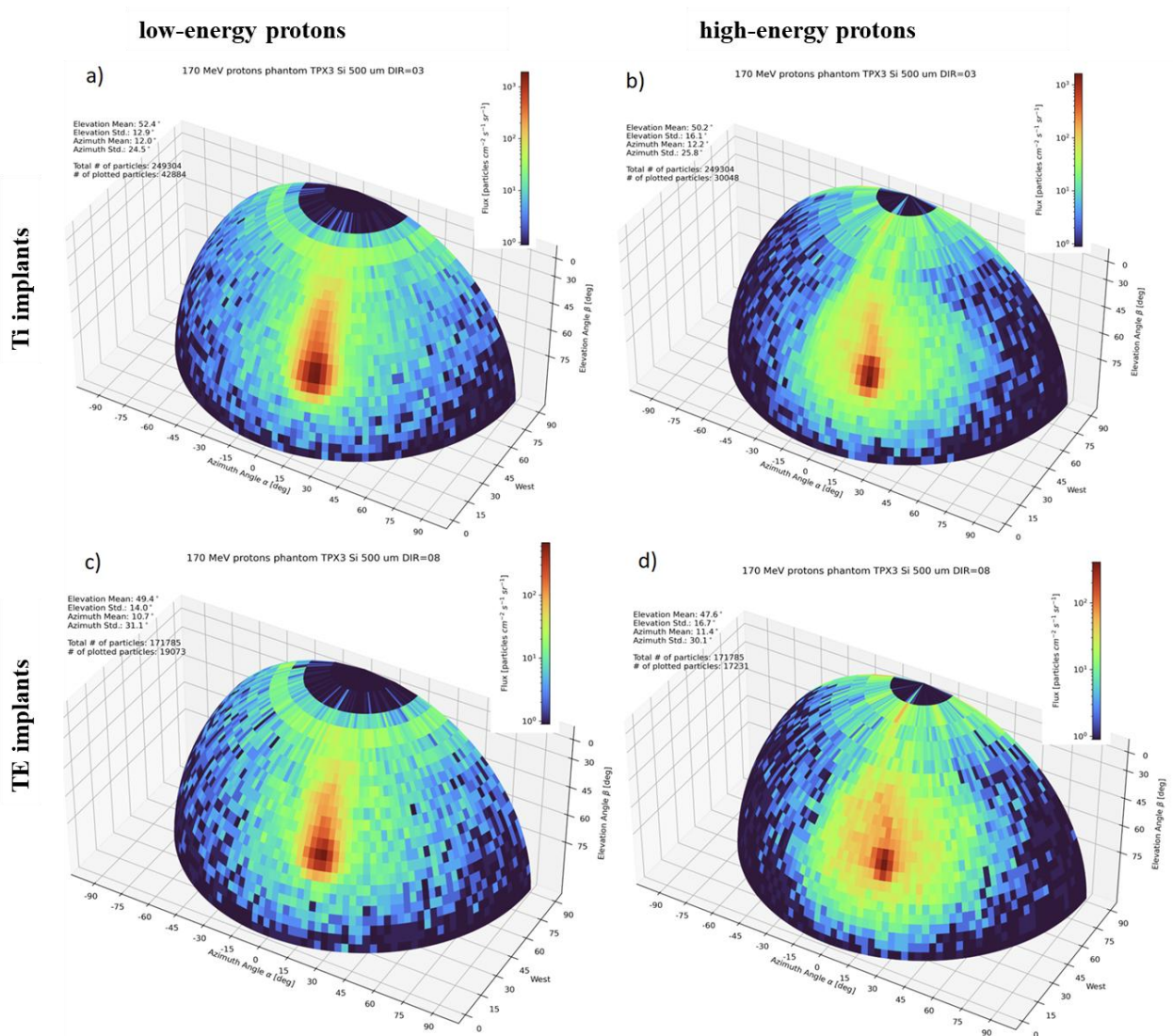


Figure 4.3 Directional maps of scattered low-energy protons (left) and high-energy protons (right) decomposed from the mixed field. These maps were created from the angular position of the Si sensor of the TPX3 at 60° relative to the beam incident, placed behind the anthropomorphic head phantom with Ti implants (first row) and tissue equivalents inserts (second row), respectively [17].

4.4 Discussion and conclusions

The presented methodology during this experiment summarizes the impact of two Ti implants in proton therapy for a head and neck case by using an anthropomorphic head phantom.

Similar to a clinical case of HNC treatment, the proposed experiment offers a detailed analysis of LET calculations into one field proton treatment plan by performing decomposition of the out-of-field radiation. The discrimination and particle identification were possible using artificial intelligence combined with neural networks trained to recognize individual tracks through the sensor thickness. Some contrasts were reported in the decomposition of the scattered protons and light particles like electrons and photons. For two angular positions of the Si sensor relative to the direction of the incident beam, three groups of particles were identified using AI NN algorithms: protons, electrons combined with photons, and ions.

Measuring the deposited energy through the sensor's thickness, scattered protons illustrated the widest spectrum of LET(water) from 0.5 up to 8 keV/ μm , being the main class of particles responsible for dose deposition behind the SOBP.

By doing this extended characterization of the out-of-field radiation distal of the SOBP, TPX3 has shown capabilities for clinical applications in proton treatments. To resolve more uncertainties correlated to possible secondary cancer induction and high levels of LET, artificial intelligence and machine learning algorithms should be integrated into precise dose calculation [17].

5. Dosimetric impact of Titanium (Ti) implants in proton therapy

5.1 Impact of titanium inserts in proton therapy

This analysis provides a dosimetric characterization of stray radiation generated by incident protons as they pass through two titanium implants positioned alongside of the Bragg curve. To achieve this, high-resolution sensors with a pixel matrix were integrated into the irradiation setup to measure the LET spectra of scattered radiation. Two MiniPIX Timepix3 detectors with Si sensors were used to evaluate and visualize the scattered particles behind Ti implants. Dedicated particle identification algorithms were applied to decompose the mixed radiation field into three groups of particles: i) protons, ii) electrons and photons, and iii) ions with fast neutrons. Dose rate, particle fluxes, and LET measurements were examined to evaluate the impact of Ti implants in proton therapy and a polymethyl methacrylate (PMMA) phantom [18].

5.2 Material and methods

Two dental Ti implants were fixed at the edge of one PMMA phantom, with a 140 mm water equivalent thickness, in the sub-peak region of an incident proton beam with an energy of 170 MeV.

The out-of-field radiation was monitored during the experiment by two miniaturized radiation cameras, MiniPIX Timepix3 with Si sensor with 300 and 500 μm thickness. Placed at 11 cm, with an angular position (45°) compared to the direction of the primary proton beam, both detectors were placed behind the PMMA phantom with the Ti implants. The measurements were done simultaneously, meaning that the TPX3 with 500 μm Si sensor monitored the radiation produced behind Ti implants, while the TPX3 detector with 300 μm

sensor, measured the contribution of the stray radiation without any metallic inhomogeneity in the beam's path.

The experimental results presented in this study correspond only to those events reported from the area chosen, $4.5 \times 14.08 \text{ mm}^2$, without any material placed on the sensor level. Taking advantage of the structural design of the TPX3 detection camera, the time of arrival and energy of single particle event were collected simultaneously [50].

TPX3 detectors are not dosimeters, meaning that the absorbed dose cannot be directly measured with this miniaturized radiation camera. Instead, TPX3 records the energy deposition of each incident particle striking the sensor, allowing the dose to be calculated from spectral acquisition. [18].

5.3 Results

Particle identification and classification

Primary and secondary particles created alongside the Bragg curve were decomposed into three classes: i) protons, ii) electrons and photons (both contributions from X-rays and low-energy gamma rays), and iii) ions (high-energy transfer particles with tracks other than proton-induced events). Complete decomposition of 3000 events registered by the TPX3 detectors in 8 s intervals for both setups, with Ti implants and without them, is presented in Figure 5.1 a. Highlighted as 2D images of deposited energy per pixel, a comparative analysis of mixed radiation field resulting from incident proton beam passing through a PMMA phantom with and without metallic inserts were measured, and quantitative analyses were performed for each setup. As shown in Figure 5.1 b, protons - representing the predominant contribution, were spotted in the scattered radiation in both setups, with minimal variations. With a difference of 66 particles, more protons were detected when the dental implants were inserted along the Bragg curve, compared to 1607 events marked in the

other situation [18]. With similar behavior, electrons and photons (see Figure 5.1 c) exhibit minor differences between setups: 1324 events identified by the TPX3 detector oriented towards Ti implants and 1356 without them. Ions represent the last group of particles recognized by the NN algorithms, Figure 5.1 d. The situation is entirely different for this category of particles. 37 particles were detected by the TPX3 detector, whose sensor faces the Ti implants, and only three particles were registered by the other TPX3 that monitors the scattered radiation without inhomogeneity inserts.

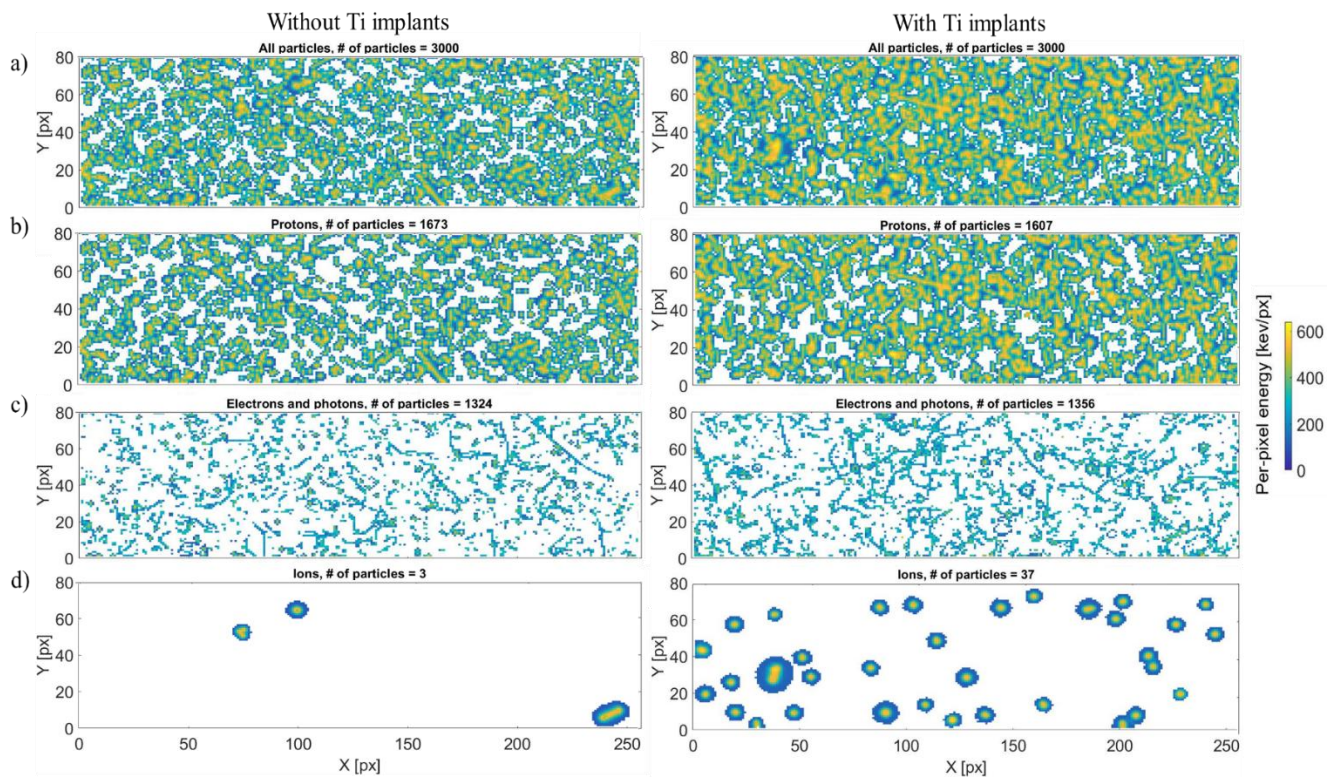


Figure 5.1 Representation of the integrated energy deposited by 3000 particles in 8 s. The decomposition of the mixed field produced by all events (a) behind the PMMA phantom without Ti implants (left) and with those two high-Z material inserts (right). Three groups of particles were defined: b) protons, c) electrons with photons and d) ions [18]

Dosimetry analysis: particle fluxes and dose rates evaluation

Particle fluxes and DR were measured in both cases, and the results of their averaged values over 200 s are presented in Figure 5.2 a and b [18].

Involving two detectors with different thicknesses, their X-ray detection efficiency was considered in data processing. Data collected with the 300 μm Si sensor TPX3 detector were adjusted to match the photon detection efficiency of the TPX3 with a 500 μm Si sensor [18], [35].

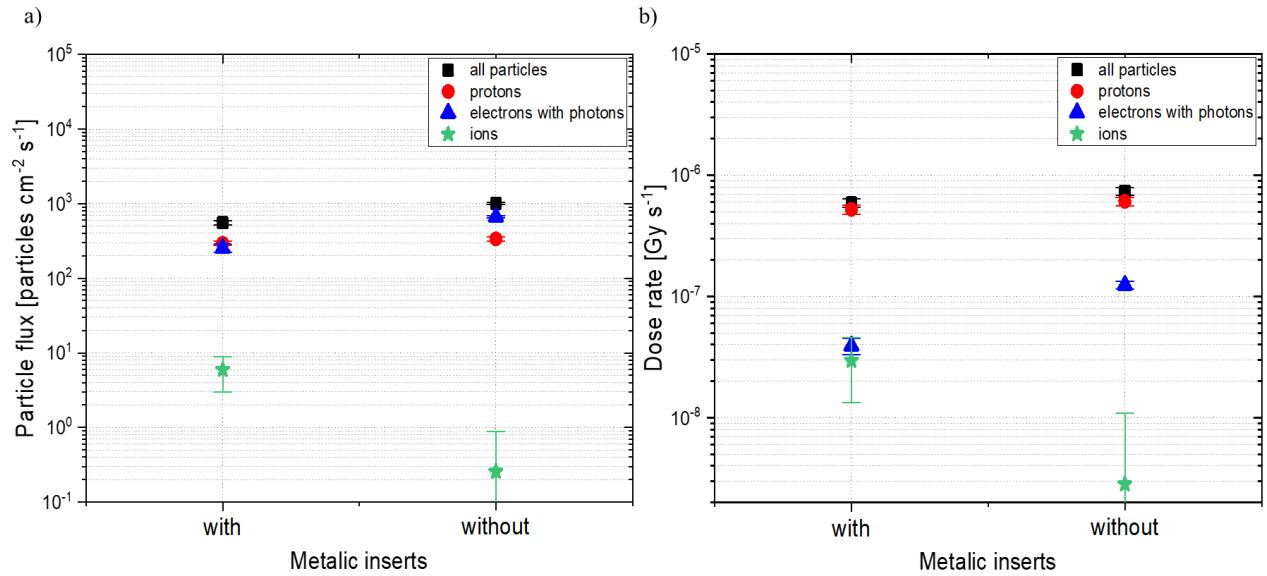


Figure 5.2 Particle fluxes (a) and dose rates (b) were measured with a TPX3 detector and a Si sensor for resolved groups of particles in both setups: with and without dental implants. Data were averaged over 200 s of continuous irradiation, with statistical deviations ($k=1$) [18]

Studying the particle fluxes behind Ti implants, the TPX3 detector registered 550.1 ± 40 particles \cdot cm⁻² \cdot s⁻¹. Conversely, the particle fluxes reported when no metallic inserts were present in the Bragg curve is almost double, with 1004.4 ± 38 particles \cdot cm⁻² \cdot s⁻¹ being counted. Nuclear interactions appeared because incident proton interactions with the Ti atoms induced a predominant number of protons in the fluxes of scattered radiation with a contribution of 337.3 ± 22 particles \cdot cm⁻² \cdot s⁻¹. Reporting a very low level of ions contribution to the flux of stray radiation highlights the lack of evidence in the current methodology for this class of particles [18].

Regardless of the presence of Ti implants, protons are the primary particles responsible for dose deposition alongside the Bragg curve: $5.22 \cdot 10^{-7}$

Gy/s measured with metallic structure and $6.07 \cdot 10^{-7}$ Gy/s without them. In the contribution of the electrons and photons to the dose rates, a one-third reduction in measured values was detected between the setups ($0.39 \cdot 10^{-7}$ Gy/s – with Ti and $1.24 \cdot 10^{-7}$ Gy/s – without Ti). For the third class of particles, generally named “ions”, placing the high-Z material into the beam’s path produces a DR of $0.29 \cdot 10^{-7}$ Gy/s, ten times higher than the other case without metallic inserts when only $0.02 \cdot 10^{-7}$ Gy/s was detected [18].

LET distribution

The directional and spectral fingerprints of each particle cluster were analyzed, and the LET calculation for all three particle classes is presented in Figure 5.3. Using TPX3 detectors equipped with Si sensors, the measured LET spectra along the Bragg Peak created by the incident proton beam with a nominal energy of 170 MeV were correlated with the sensor thickness specific for each case. The experimental LET measured in Si (LET_{Si}) for the setup with Ti implants is highlighted in blue, while the other is marked with red. Individual LET_{Si} spectra for each decomposed group of particles were done [18].

With a spectrum from 0.5 up to 8.5 keV/ μ m, protons are characterized by a broad LET_{Si} spectrum regardless of the presence of the metallic structures in the irradiation field (see Figure 5.3. b). Without Ti implants, one distinctive region could be observed at 1.5 keV/ μ m when more protons with this level of LET_{Si} were detected. With a maximum value of 0.75 keV/ μ m, scattered protons presented behind the phantom with Ti implants result for multiple Coulomb scattering events merged with nonelastic nuclear interactions reported in the sub-peak region [18], [56]. The lowest LET_{Si} was assigned to the electrons and photons group, resulting in values up to 2 keV/ μ m for both situations, as Figure 5.3 c shows. Placing the Ti implants into the beam’s path, more electrons and X-ray particles are attenuated, and their energy transfer is reduced in 1-2 keV/ μ m intervals. Known as nuclear interaction results from primary protons

interactions with heavy atoms, more ions were formed with LET_{Si} ranges from 4 up to $6.5 \text{ keV}/\mu\text{m}$, as Figure 5.3. presents. These results highlight the considerable influence over the LET distribution in the presence of metallic structures. The composition of the scattered radiation is considerably modified, and increased energy transfer levels show amplified dynamics in ionizing particle distribution when Ti inserts are included in the beam's delivery [18].

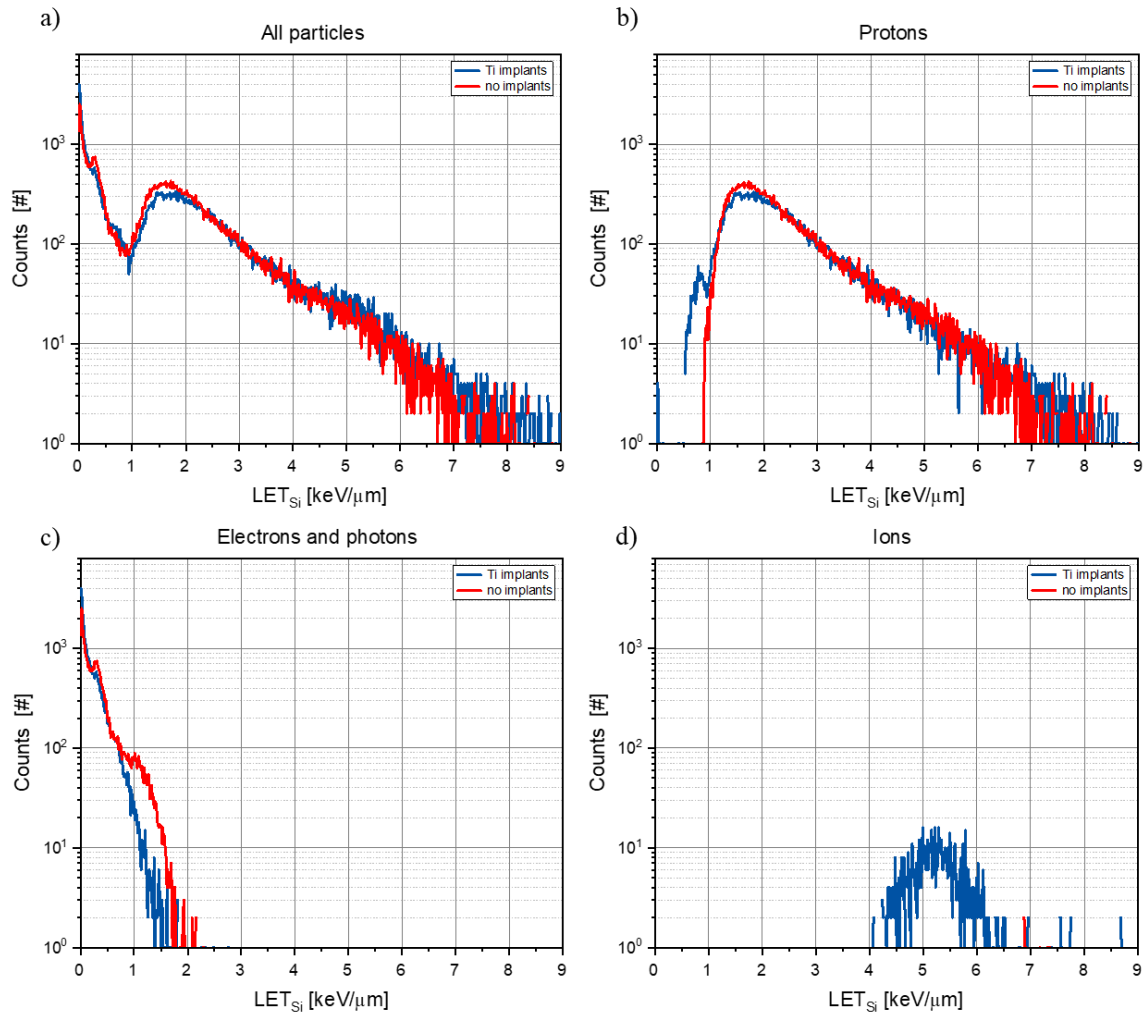


Figure 5.3 LET spectra in Si for scattered radiation in both cases: with (blue) and without (red) implants measured with TPX3 detectors (a). The decomposition of mixed radiation allowed individual evaluation of LET spectra for all three groups of particles: b) protons, c) electrons with photons and d) ions [18]

5.4 Discussion and conclusions

The proposed study presents dosimetric fluctuations recorded in proton therapy with Ti implants employing high-resolution Timpix3 detectors. Simulating a clinical environment during the measurements, the decomposition of the out-of-field was done in two cases, with and without the dental Ti implants attached to the PMMA phantom. Separately, for three groups of particles (protons, electrons and photons, ions), a comprehensive analysis of fluxes, dose rate and LET spectra was generated. Distinctive patterns in mixed field composition and their contribution to the scattered radiation dose deposition alongside the Bragg peak were observed in both situations presented in this section. Due to the specific interactions between incident protons and the heavier atoms in metallic inserts, the presence of these structures in the beam's path alters the composition of scattered radiation, especially influencing ion production. More ions were generated with Ti implants, but scattered protons remained the predominant particles identified during the flux and dose rate monitoring. Correlating these results underscores the importance of considering metallic structures in particle therapy treatment planning, ensuring optimal dose delivery while minimizing risks to healthy tissue [18].

General conclusions

The findings presented in this thesis highlight the feasibility of TPX3 detectors for characterizing the radiation produced in particle therapy. As highly suitable radiation detectors for beam monitoring in UHDR conditions, this category of miniaturized radiation camera demonstrated their applicability in measuring both primary and scattered FLASH electron radiation up to 16 cm away from the beam's core. Moreover, TPX3 detectors successfully registered the stray radiation beyond the Spread-Out Bragg peak and from the sub-peak region of the Bragg peak, focusing on particle identification and spectral discrepancies with and without Ti implants.

In the current methodology, neutron tracks overlap with those created by protons, necessitating further research on neutron-proton discrimination in out-of-field radiation characterization. Future improvements in neural network-based recognition methods, incorporating more complex cluster features such as deposited energy and derived LET, could enhance particle identification. In this context, an enhanced overview of higher LET particle's interaction with healthy tissue and their impact on the dose deposition at this level will provide valuable insights into the potential risks of secondary cancer induction.

Personal contributions included as part of the thesis

List of publications indexed in ISI- journals

- C. Oancea, C. Bălan, J. Pivec, C. Granja, J. Jakubek, D. Chvatil, V. Olsansky and V. Chiş, “Stray radiation produced in FLASH electron beams characterized by the MiniPIX Timepix3 Flex detector”, *Journal of Instrumentation*, vol. 17, no. 01, p. C01003, 2022, doi: [10.1088/1748-0221/17/01/C01003](https://doi.org/10.1088/1748-0221/17/01/C01003).

IF: 1.3, AIS: 0.438

- C. Bălan, C. Granja, G. Mytsin, S. Shvidky, A. Molokanov, L. Marek, V. Chiş and C. Oancea, “Particle tracking, recognition and LET evaluation of out-of-field proton therapy delivered to a phantom with implants”, *Phys Med Biol*, vol. 69, no. 16, p. 165006, 2024, doi: [10.1088/1361-6560/AD61B8](https://doi.org/10.1088/1361-6560/AD61B8).

IF: 3.3, AIS: 0.893

- C. Bălan, C. Granja, G. Mytsin, S. Shvidky, A. Molokanov, V. Chiş and C. Oancea, “Assessing the dosimetric effects of high-Z titanium implants in proton therapy using pixel detectors”, *Journal of Instrumentation*, vol. 20, no. 01, p. C01002, 2025, doi: [10.1088/1748-0221/20/01/C01002](https://doi.org/10.1088/1748-0221/20/01/C01002)

IF: 1.3, AIS: 0.425

International conference participation

Oral presentation

- C. Bălan, C. Granja, G. Mytsin, S. Shvidky, A. Molokanov, V. Chiş and C. Oancea, 25th International Workshop on Radiation Imaging Detectors, Lisbon, June 30 – July 4, 2024; “High-resolution characterization of scattered radiation in proton therapy by Timepix3 detectors behind phantoms with and without dental implants”

Poster presentation

- **C. Bălan**, C. Oancea, J. Pivec, C. Granja, J. Jakubek, D. Chvatil, V. Olsansky, V. Chiș, *22nd International Workshop on Radiation Imaging Detectors, Brussels (online), June 27 – July 1, 2021*; “Characterization of stray radiation produced in FLASH electron beams using customized MiniPIX Timepix3 detectors”
- **C. Bălan**, C. Oancea, J. Pivec, C. Granja, J. Jakubek, D. Chvatil, V. Olsansky, V. Chiș, *FLASH Radiotherapy and Particle Therapy Conference, online, December 1-3, 2021*; “Measurements of scattered radiation produced in electron beams using MiniPIX Timepix3 Flex”
- C. Oancea, **C. Bălan**, D. Chvatil, C. Granja, J. Jakubek, V. Olsansky, J. Pivec, *FLASH Radiotherapy and Particle Therapy Conference, online, December 1-3, 2021*; “Time-stamped measurements of single FLASH pulses of Primary Electron Beams in wide dose range and microseconds resolution with miniaturized MiniPIX Timepix3 Camera”
- **C. Bălan**, C. Granja, G. Mytsin, S. Shvidky, A. Molokanov, V. Chiș and C. Oancea, *American Society for Radiation Oncology (ASTRO) 64th Annual Meeting, San Antonio (online), October 22-26, 2022*; “Characterization of stray radiation produced by a proton beam in an anthropomorphic phantom with dental implants using a Timepix3 detector”
- **C. Bălan**, C. Granja, G. Mytsin, S. Shvidky, A. Molokanov, V. Chiș, C. Oancea, *School of Hadron Radiotherapy, Trieste, April 8-12, 2024*; “Scattered radiation morphology and spectral analyses produced by a proton beam in a head and neck case with dental implants” – awarded with “The best poster” prize

National conference participation

Oral presentation

- **C. Bălan**, C. Oancea, J. Pivec, C. Granja, J. Jakubek, D. Chvatil, V. Olsansky, V. Chiș, *A XIX-a Conferință Națională de Fizică Medicală (CNFMR), online, November 6-7, 2021; "Caracterizarea radiației secundare produse de un fascicol de electroni FLASH cu ajutorul detectorilor Timepix3"*
- **C. Bălan**, C. Oancea, C. Granja, G. Mytsin, S. Shvidky, A. Molokanov, V. Chiș, *A XX-a Conferință Națională de Fizică Medicală (CNFMR), Oradea, November 4-5, 2022; "Caracterizarea radiației produsă de un fascicol de protoni într-un fantom antropomorf cu implanturi dentare folosind detectori Timepix3"*
- **C. Bălan**, C. Granja, C. Oancea, G. Mytsin, S. Shvidky, A. Molokanov, V. Chiș, *Al 34-lea Congres al Societății Române de Radioterapie și Oncologie Medicală, Cluj-Napoca, November 2-5, 2023; "Dosimetric characterization of scattered radiation produced by a proton beam using Timepix3 detectors in a head and neck case with dental implants"*

Additional contributions not related to the PhD subject

List of publications indexed in ISI- journals

- A. Turcas, D. Leucuta, **C. Bălan**, *et al*, “Deep-learning magnetic resonance imaging-based automatic segmentation for organs-at-risk in the brain: Accuracy and impact on dose distribution”, *PhiRO*, vol. 27, 2023, doi: [10.1016/j.phro.2023.100454](https://doi.org/10.1016/j.phro.2023.100454)
IF: 3.4, AIS: 0.767
- A. Turcas, B. Homorozeanu, C. Gheara, **C. Bălan**, *et al*, “Dynamics and predictors of hematologic toxicity during crano-spinal irradiation”, *Reports of Practical Oncology and Radiotherapy*, vol. 29, 2024, doi: [10.5603/rpor.101094](https://doi.org/10.5603/rpor.101094)
IF: 1.2, AIS: 0.286

Oral presentation (national conference)

- **C. Bălan**, O. Diaconu, D. Martin, *Al 34-lea Congres al Societății Române de Radioterapie și Oncologie Medicală, Cluj-Napoca, November 2-5, 2023*; “Are Hybrid Techniques Feasible for Treating Breast Cancer Patients? An institutional study of dosimetric aspects in treatment planning”
- O. Diaconu, **C. Bălan**, D. Martin, *Al 34-lea Congres al Societății Române de Radioterapie și Oncologie Medicală, Cluj-Napoca, November 2-5, 2023*; “Preclinical Evaluation of *in-vivo* dosimetry for external beam radiotherapy. A breast cancer study in an anthropomorphic phantom”

Poster presentation (national conference)

- E. Nedelcu, **C. Bălan**, V. Chiș, *Al 34-lea Congres al Societății Române de Radioterapie și Oncologie Medicală, Cluj-Napoca, November 2-5, 2023*; “Evaluation of delivered dose during the pre-treatment positioning in radiotherapy using *in-vivo* dosimetry system”

- A. Someșan, **C. Bălan**, *Al 34-lea Congres al Societății Române de Radioterapie și Oncologie Medicală, Cluj-Napoca, November 2-5, 2023; “ The impact of the effective point of measurements in relative dosimetry”*

Bibliography

- [1] R. A. Chandra, F. K. Keane, F. E. M. Voncken, and C. R. Thomas, “Contemporary radiotherapy: present and future,” *The Lancet*, vol. 398, no. 10295, pp. 171–184, Jul. 2021, doi: [10.1016/S0140-6736\(21\)00233-6](https://doi.org/10.1016/S0140-6736(21)00233-6)
- [2] P. Freisleder *et al.*, “Recent advances in Surface Guided Radiation Therapy,” *Radiation Oncology*, vol. 15, no. 1, p. 187, Dec. 2020, doi: [10.1186/s13014-020-01629-w](https://doi.org/10.1186/s13014-020-01629-w)
- [3] M. C. Vozenin, J. Bourhis, and M. Durante, “Towards clinical translation of FLASH radiotherapy,” *Nat Rev Clin Oncol*, vol. 19, no. 12, pp. 791–803, Oct. 2022, doi: [10.1038/s41571-022-00697-z](https://doi.org/10.1038/s41571-022-00697-z)
- [4] A. Castellano *et al.*, “Advanced Imaging Techniques for Radiotherapy Planning of Gliomas,” *Cancers (Basel)*, vol. 13, no. 5, p. 1063, Mar. 2021, doi: [10.3390/CANCERS13051063](https://doi.org/10.3390/CANCERS13051063)
- [5] C. Oancea *et al.*, “High-count-rate particle tracking in proton and carbon radiotherapy with Timepix2 operated in ultra-short acquisition time,” *Journal of Instrumentation*, vol. 19, no. 11, p. C11002, Nov. 2024, doi: [10.1088/1748-0221/19/11/C11002](https://doi.org/10.1088/1748-0221/19/11/C11002)
- [6] L. Vanderwaeren, R. Dok, K. Verstrepen, and S. Nuyts, “Clinical Progress in Proton Radiotherapy: Biological Unknowns,” *Cancers 2021*, vol. 13, no. 4, p. 604, Feb. 2021, doi: [10.3390/CANCERS13040604](https://doi.org/10.3390/CANCERS13040604)
- [7] F. Romano, C. Bailat, P. G. Jorge, M. L. F. Lerch, and A. Darafsheh, “Ultra-high dose rate dosimetry: Challenges and opportunities for FLASH radiation therapy,” *Med Phys*, vol. 49, no. 7, pp. 4912–4932, Jul. 2022, doi: [10.1002/MP.15649](https://doi.org/10.1002/MP.15649)
- [8] A. Vignati *et al.*, “Beam Monitors for Tomorrow: The Challenges of Electron and Photon FLASH RT,” *Front Phys*, vol. 8, p. 577984, Sep. 2020, doi: [10.3389/fphy.2020.00375](https://doi.org/10.3389/fphy.2020.00375)
- [9] C. Granja *et al.*, “MiniPIX Timepix3 — a miniaturized radiation camera with onboard data processing for online characterization of wide-intensity mixed-radiation fields,” *Journal of Instrumentation*, vol. 17, no. 03, p. C03019, Mar. 2022, doi: [10.1088/1748-0221/17/03/C03019](https://doi.org/10.1088/1748-0221/17/03/C03019)
- [10] F. Kalholm, L. Grzanka, E. Traneus, and N. Bassler, “A systematic review on the usage of averaged LET in radiation biology for particle therapy,”

- Radiotherapy and Oncology*, vol. 161, pp. 211–221, Aug. 2021, doi: [10.1016/J.RADONC.2021.04.007](https://doi.org/10.1016/J.RADONC.2021.04.007)
- [11] H. K. Byun *et al.*, “Physical and Biological Characteristics of Particle Therapy for Oncologists,” *Cancer Research and Treatment : Official Journal of Korean Cancer Association*, vol. 53, no. 3, p. 611, Jul. 2021, doi: [10.4143/CRT.2021.066](https://doi.org/10.4143/CRT.2021.066)
- [12] R. Panthi, P. Maggi, S. Peterson, D. MacKin, J. Polf, and S. Beddar, “Secondary Particle Interactions in a Compton Camera Designed for in vivo Range Verification of Proton Therapy,” *IEEE Trans Radiat Plasma Med Sci*, vol. 5, no. 3, pp. 383–391, May 2021, doi: [10.1109/TRPMS.2020.3030166](https://doi.org/10.1109/TRPMS.2020.3030166)
- [13] “Home | medipix.web.cern.ch.” Accessed: Sep. 29, 2024. [Online]. Available: <https://medipix.web.cern.ch/>
- [14] C. Oancea *et al.*, “Thermal neutron detection and track recognition method in reference and out-of-field radiotherapy FLASH electron fields using Timepix3 detectors,” *Phys Med Biol*, vol. 68, no. 18, p. 185017, Sep. 2023, doi: [10.1088/1361-6560/ACF2E1](https://doi.org/10.1088/1361-6560/ACF2E1)
- [15] C. Oancea *et al.*, “Out-of-field measurements and simulations of a proton pencil beam in a wide range of dose rates using a Timepix3 detector: Dose rate, flux and LET,” *Physica Medica*, vol. 106, p. 102529, Feb. 2023, doi: [10.1016/J.EJMP.2023.102529](https://doi.org/10.1016/J.EJMP.2023.102529)
- [16] C. Oancea *et al.*, “Stray radiation produced in FLASH electron beams characterized by the MiniPIX Timepix3 Flex detector,” *Journal of Instrumentation*, vol. 17, no. 01, p. C01003, Jan. 2022, doi: [10.1088/1748-0221/17/01/C01003](https://doi.org/10.1088/1748-0221/17/01/C01003)
- [17] C. Bălan *et al.*, “Particle tracking, recognition and LET evaluation of out-of-field proton therapy delivered to a phantom with implants,” *Phys Med Biol*, vol. 69, no. 16, p. 165006, Jul. 2024, doi: [10.1088/1361-6560/AD61B8](https://doi.org/10.1088/1361-6560/AD61B8)
- [18] C. Bălan *et al.*, “Assessing the dosimetric effects of high-Z titanium implants in proton therapy using pixel detectors,” *Journal of Instrumentation*, vol. 20, no. 01, p. C01002, Jan. 2025, doi: [10.1088/1748-0221/20/01/C01002](https://doi.org/10.1088/1748-0221/20/01/C01002)
- [19] D. van der Merwe *et al.*, “Accuracy requirements and uncertainties in radiotherapy: a report of the International Atomic Energy Agency,” *Acta Oncol (Madr)*, vol. 56, no. 1, pp. 1–6, Jan. 2017, doi: [10.1080/0284186X.2016.1246801](https://doi.org/10.1080/0284186X.2016.1246801)
- [20] J. P. Gibbons, *Khan’s the physics of radiation therapy*. Wolters Kluwer, 2019.

- [21] D. De Ruyscher, G. Niedermann, N. G. Burnet, S. Siva, A. W. M. Lee, and F. Hegi-Johnson, "Radiotherapy toxicity," *Nat Rev Dis Primers*, vol. 5, no. 1, pp. 1–20, Feb. 2019, doi: [10.1038/s41572-019-0064-5](https://doi.org/10.1038/s41572-019-0064-5)
- [22] O. V. Gul, "Experimental evaluation of out-of-field dose for different high-energy electron beams and applicators used in external beam radiotherapy," *Radiation Physics and Chemistry*, vol. 215, p. 111345, Feb. 2024, doi: [10.1016/J.RADPHYSICHEM.2023.111345](https://doi.org/10.1016/J.RADPHYSICHEM.2023.111345)
- [23] P. Stasica *et al.*, "Single proton LET characterization with the Timepix detector and artificial intelligence for advanced proton therapy treatment planning," *Phys Med Biol*, vol. 68, no. 10, p. 104001, May 2023, doi: [10.1088/1361-6560/ACC9F8](https://doi.org/10.1088/1361-6560/ACC9F8)
- [24] M. Missiaggia, G. Cartechini, F. Tommasino, E. Scifoni, and C. La Tessa, "Investigation of In-Field and Out-of-Field Radiation Quality With Microdosimetry and Its Impact on Relative Biological Effectiveness in Proton Therapy," *International Journal of Radiation Oncology*Biophysics*, vol. 115, no. 5, pp. 1269–1282, Apr. 2023, doi: [10.1016/J.IJROBP.2022.11.037](https://doi.org/10.1016/J.IJROBP.2022.11.037)
- [25] D. S. Chang, F. D. Lasley, I. J. Das, M. S. Mendonca, and J. R. Dynlacht, *Basic Radiotherapy Physics and Biology*. Cham: Springer International Publishing, 2021, doi: [10.1007/978-3-030-61899-5](https://doi.org/10.1007/978-3-030-61899-5)
- [26] P. P. Connell and S. Hellman, "Advances in Radiotherapy and Implications for the Next Century: A Historical Perspective," *Cancer Res*, vol. 69, no. 2, pp. 383–392, Jan. 2009, doi: [10.1158/0008-5472.CAN-07-6871](https://doi.org/10.1158/0008-5472.CAN-07-6871)
- [27] C. L. Limoli and M.-C. Vozenin, "Reinventing Radiobiology in the Light of FLASH Radiotherapy," *Annu Rev Cancer Biol*, vol. 7, no. 1, pp. 1–21, Apr. 2023, doi: [10.1146/annurev-cancerbio-061421-022217](https://doi.org/10.1146/annurev-cancerbio-061421-022217)
- [28] C. M. . Washington and D. T. Leaver, *Principles and practice of radiation therapy*, 4th ed. Elsevier Mosby, 2016.
- [29] F. H. Attix, *Introduction to Radiological Physics and Radiation Dosimetry*. Wiley, 1986, doi: [10.1002/9783527617135](https://doi.org/10.1002/9783527617135)
- [30] H. Thomas and B. Timmermann, "Paediatric proton therapy," *British Journal of Radiology*, vol. 93, no. 1107, Mar. 2020, doi: [10.1259/BJR.20190601/7449271](https://doi.org/10.1259/BJR.20190601/7449271)
- [31] J. E. Leeman *et al.*, "Proton therapy for head and neck cancer: expanding the therapeutic window," *Lancet Oncol*, vol. 18, no. 5, pp. e254–e265, May 2017, doi: [10.1016/S1470-2045\(17\)30179-1](https://doi.org/10.1016/S1470-2045(17)30179-1)

- [32] V. Gondi, T. I. Yock, and M. P. Mehta, "Proton therapy for paediatric CNS tumours – improving treatment-related outcomes," *Nature Reviews Neurology* 2016 12:6, vol. 12, no. 6, pp. 334–345, May 2016, doi: [10.1038/nrneurol.2016.70](https://doi.org/10.1038/nrneurol.2016.70)
- [33] W. D. Newhauser and R. Zhang, "The physics of proton therapy," *Phys Med Biol*, vol. 60, no. 8, p. R155, Mar. 2015, doi: [10.1088/0031-9155/60/8/R155](https://doi.org/10.1088/0031-9155/60/8/R155)
- [34] B. Gottschalk, "Physics of Proton Interactions in Matter," in *Proton Therapy Physics*, CRC Press, pp. 27–66, 2018, doi: [10.1201/b22053-3](https://doi.org/10.1201/b22053-3)
- [35] C. Granja *et al.*, "Resolving power of pixel detector Timepix for wide-range electron, proton and ion detection," *Nucl Instrum Methods Phys Res A*, vol. 908, pp. 60–71, Nov. 2018, doi: [10.1016/J.NIMA.2018.08.014](https://doi.org/10.1016/J.NIMA.2018.08.014)
- [36] R. Ballabriga, M. Campbell, and X. Llopart, "Asic developments for radiation imaging applications: The medipix and timepix family," *Nucl Instrum Methods Phys Res A*, vol. 878, pp. 10–23, Jan. 2018, doi: [10.1016/J.NIMA.2017.07.029](https://doi.org/10.1016/J.NIMA.2017.07.029)
- [37] R. Al Darwish, L. Marcu, and E. Bezak, "Overview of current applications of the Timepix detector in spectroscopy, radiation and medical physics," *Appl Spectrosc Rev*, vol. 55, no. 3, pp. 243–261, Mar. 2020, doi: [10.1080/05704928.2019.1580202](https://doi.org/10.1080/05704928.2019.1580202)
- [38] M. Urban, O. Nentvich, L. Marek, R. Hudec, and L. Sieger, "Timepix3: Temperature Influence on Radiation Energy Measurement with Si Sensor," *Sensors*, vol. 23, no. 4, p. 2201, Feb. 2023, doi: [10.3390/S23042201](https://doi.org/10.3390/S23042201)
- [39] C. Granja, M. Davidkova, J. Vilimovsky, and V. Vondracek, "Quantum-imaging detection of secondary neutrons in proton radiotherapy fields," *Journal of Instrumentation*, vol. 18, no. 11, p. C11011, Nov. 2023, doi: [10.1088/1748-0221/18/11/C11011](https://doi.org/10.1088/1748-0221/18/11/C11011)
- [40] C. Granja *et al.*, "Energy loss and online directional track visualization of fast electrons with the pixel detector Timepix," *Radiat Meas*, vol. 59, pp. 245–261, Dec. 2013, doi: [10.1016/J.RADMEAS.2013.07.006](https://doi.org/10.1016/J.RADMEAS.2013.07.006)
- [41] C. Granja *et al.*, "Directional detection of charged particles and cosmic rays with the miniaturized radiation camera MiniPIX Timepix," *Nucl Instrum Methods Phys Res A*, vol. 911, pp. 142–152, Dec. 2018, doi: [10.1016/J.NIMA.2018.09.140](https://doi.org/10.1016/J.NIMA.2018.09.140)
- [42] B. Hartmann *et al.*, "Distortion of the per-pixel signal in the Timepix detector observed in high energy carbon ion beams1," *Journal of*

- Instrumentation*, vol. 9, no. 09, p. P09006, Sep. 2014, doi: [10.1088/1748-0221/9/09/P09006](https://doi.org/10.1088/1748-0221/9/09/P09006)
- [43] C. Granja *et al.*, “Dynamic range and resolving power of the Timepix detector to heavy charged particles,” *Journal of Instrumentation*, vol. 13, no. 11, pp. C11003–C11003, Nov. 2018, doi: [10.1088/1748-0221/13/11/C11003](https://doi.org/10.1088/1748-0221/13/11/C11003)
- [44] L. S. Pinsky and S. Pospisil, “Timepix-based detectors in mixed-field charged-particle radiation dosimetry applications,” Nov. 01, 2020, *Elsevier Ltd.*, doi: [10.1016/j.radmeas.2019.106229](https://doi.org/10.1016/j.radmeas.2019.106229)
- [45] “ADVACAM Radiation Imaging Solutions – Semiconductor Photon Counting Cameras.” Accessed: Dec. 28, 2024. [Online]. Available: <https://advacam.com/>
- [46] X. Llopart, R. Ballabriga, M. Campbell, L. Tlustos, and W. Wong, “Timepix, a 65k programmable pixel readout chip for arrival time, energy and/or photon counting measurements,” *Nucl Instrum Methods Phys Res A*, vol. 581, no. 1–2, pp. 485–494, Oct. 2007, doi: [10.1016/J.NIMA.2007.08.079](https://doi.org/10.1016/J.NIMA.2007.08.079)
- [47] M. Sommer, C. Granja, S. Kodaira, and O. Ploc, “High-energy per-pixel calibration of timepix pixel detector with laboratory alpha source,” *Nucl Instrum Methods Phys Res A*, vol. 1022, p. 165957, Jan. 2022, doi: [10.1016/J.NIMA.2021.165957](https://doi.org/10.1016/J.NIMA.2021.165957)
- [48] L. Marek *et al.*, “Data Processing Engine (DPE): data analysis tool for particle tracking and mixed radiation field characterization with pixel detectors Timepix,” *Journal of Instrumentation*, vol. 19, no. 04, p. C04026, Apr. 2024, doi: [10.1088/1748-0221/19/04/C04026](https://doi.org/10.1088/1748-0221/19/04/C04026)
- [49] M. R. Ashraf *et al.*, “Dosimetry for FLASH Radiotherapy: A Review of Tools and the Role of Radioluminescence and Cherenkov Emission,” *Front Phys*, vol. 8, p. 570033, Aug. 2020, doi: [10.3389/fphy.2020.00328](https://doi.org/10.3389/fphy.2020.00328)
- [50] T. Poikela *et al.*, “Timepix3: a 65K channel hybrid pixel readout chip with simultaneous ToA/ToT and sparse readout,” *Journal of Instrumentation*, vol. 9, no. 05, p. C05013, May 2014, doi: [10.1088/1748-0221/9/05/C05013](https://doi.org/10.1088/1748-0221/9/05/C05013)
- [51] C. Oancea *et al.*, “Radiation Measurements Using Timepix3 with Silicon Sensor and Bare Chip in Proton Beams for FLASH Radiotherapy,” Oct. 2024, Accessed: Jan. 08, 2025. [Online]. Available: <https://arxiv.org/abs/2410.00549>
- [52] P. Blanchard, G. B. Gunn, A. Lin, R. L. Foote, N. Y. Lee, and S. J. Frank, “Proton Therapy for Head and Neck Cancers,” *Semin Radiat Oncol*, vol. 28, no. 1, pp. 53–63, Jan. 2018, doi: [10.1016/J.SEMRADONC.2017.08.004](https://doi.org/10.1016/J.SEMRADONC.2017.08.004)

- [53] X. Li, A. Lee, M. A. Cohen, E. J. Sherman, and N. Y. Lee, "Past, present and future of proton therapy for head and neck cancer," *Oral Oncol*, vol. 110, p. 104879, Nov. 2020, doi: [10.1016/J.ORALONCOLOGY.2020.104879](https://doi.org/10.1016/j.oraloncol.2020.104879)
- [54] M. Zarifi, S. Guatelli, D. Bolst, B. Hutton, A. Rosenfeld, and Y. Qi, "Characterization of prompt gamma-ray emission with respect to the Bragg peak for proton beam range verification: A Monte Carlo study," *Physica Medica*, vol. 33, pp. 197–206, Jan. 2017, doi: [10.1016/J.EJMP.2016.12.011](https://doi.org/10.1016/j.ejmp.2016.12.011)
- [55] Y. Matsuzaki, H. Date, K. L. Sutherland, and Y. Kiyonagi, "Nuclear collision processes around the Bragg peak in proton therapy," *Radiol Phys Technol*, vol. 3, no. 1, pp. 84–92, Jan. 2010, doi: [10.1007/s12194-009-0081-2](https://doi.org/10.1007/s12194-009-0081-2)
- [56] J. M. Verburg and J. Seco, "Dosimetric accuracy of proton therapy for chordoma patients with titanium implants," *Med Phys*, vol. 40, no. 7, p. 071727, Jul. 2013, doi: [10.1118/1.4810942](https://doi.org/10.1118/1.4810942)